A Microwave Sensor Based on Concentric Split-Ring Resonators for Blood Urea Detection: A Novel Tool for Chronic Kidney Disease Diagnosis

Mateus I.O. Souza, Natália M. Santos, Laudemir C. Varanda, Vinicius M. Pepino, and Ben-Hur V. Borges

***Abstract*—Chronic kidney disease (CKD) affects millions of people worldwide, making early diagnosis critical for effective management and healthcare cost reduction. Monitoring blood urea levels is essential for this purpose. In this article, we present a microwave (MW) sensor capable of detecting urea concentrations within the clinical range required for CKD diagnosis, a sensitivity not achieved by previous MW-based approaches. The proposed device operates without reagents or enzymes, requires no specialized personnel, and offers an extended lifespan, ease of use, and sensitivity comparable to conventional optical sensors. Our work consists of two main steps. First, we conducted a dielectric characterization of artificial blood plasma solution (ABPS) and urea-enriched ABPS (ABPSU, 320 mg/dL) over a frequency range of 500 MHz to 10 GHz. The results revealed that the most significant differentiation between samples occurs at low frequencies, particularly in the loss tangent rather than in the real part of the dielectric constant, thereby identifying the optimal frequency range for sensor design. In the second step, we designed a double concentric circular split-ring resonator (DCCSRR) on a 49 × 45 mm Rogers 5880 substrate. A dedicated optimization protocol enhanced both the resonance peak amplitude and the quality factor of the sensor's fundamental mode. After fabrication, the DCCSRR was tested for urea concentrations ranging from 10 to 320 mg/dL, exhibiting measurable variations in S_{21} (dB) and frequency shifts around 575 MHz. This study establishes the first MW sensor operating within the urea concentration range necessary for CKD diagnosis, paving the way for practical MW-based urea monitoring.**

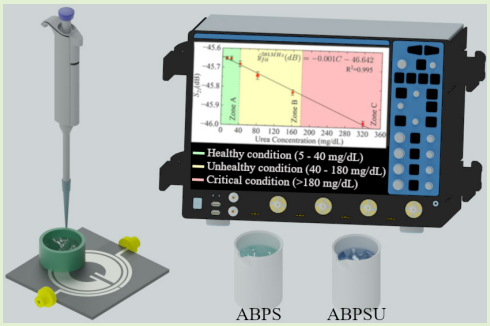

***Index Terms*— Chronic kidney diseases (CKDs) diagnosis, microwave (MW) sensors, optimization, urea sensing.**

Received 23 April 2025; accepted 5 May 2025. Date of publication 20 May 2025; date of current version 2 July 2025. This work was supported in part by the Coordination for the Improvement of Higher Education Personnel (CAPES) under Grant 001, in part by the National Council of Scientific and Technological Development (CNPq) under Grant 304208/2021-3, and in part by São Paulo Research Foundation (FAPESP) under Grant 2013/07276-1 and Grant 2020/06501-5. The associate editor coordinating the review of this article and approving it for publication was Prof. Mohammad Hossein Zarifi. *(Corresponding author: Ben-Hur V. Borges.)*

Mateus I.O. Souza, Vinicius M. Pepino, and Ben-Hur V. Borges are with the Department of Electrical Engineering and Computing, School of Engineering of São Carlos, University of São Paulo, São Carlos Campus, São Carlos, São Paulo 13566-590, Brazil (e-mail: mateusafk@usp.br; vinicius.pepino@usp.br; benhur@sc.usp.br).

Natália M. Santos and Laudemir C. Varanda are with the Department of Physical-Chemistry, Institute of Chemistry of São Carlos, University of São Paulo, São Carlos Campus, São Carlos, São Paulo 13566-590, Brazil (e-mail: nmsantos@usp.br; lvaranda@iqsc.usp.br).

This article has supplementary downloadable material available at https://doi.org/10.1109/JSEN.2025.3570067, provided by the authors.

Digital Object Identifier 10.1109/JSEN.2025.3570067

I. Introduction

CHRONIC kidney disease (CKD) has emerged as a major public health concern in 2024, affecting approximately 850 million people worldwide [1]. This condition predominantly impacts low-income families in lower-middle-income countries, where access to diagnosis, prevention, and treatment is limited [2]; moreover, 90% of those affected are unaware of their condition, further exacerbating the problem. Projections indicate that by 2040, CKD will become the fifth leading cause of years of life lost (YLL) globally [3]. In 2016, the United States spent over USD 25 billion on dialysis-related expenditures, a cost that is expected to rise over time [4].

The kidneys play an essential role in the human body by removing excess water and waste products from the blood. CKD occurs when they fail to perform these functions adequately. Depending on the stage of the disease, patients may require either a kidney transplant or dialysis. Currently,

© 2025 The Authors. This work is licensed under a Creative Commons Attribution 4.0 License.
For more information, see https://creativecommons.org/licenses/by/4.0/

the median survival for living donor transplants is estimated to be 19.2 years, whereas for deceased donor transplants, it decreases to 11.7 years [5]. In spite of these encouraging survival rates, finding a compatible organ can involve lengthy waiting times, and even posttransplant patients remain at risk for complications such as bleeding, infection, and rejection [6], [7], [8]. Dialysis, in which a machine filters and returns the blood to the patient, typically requires three sessions per week, each lasting up to four hours, and is often accompanied by side effects like fatigue, intradialytic hypotension, cramps, and dizziness [9], [10]. Given these challenges, early detection of CKD is critical for slowing disease progression.

The blood urea nitrogen (BUN) test is the standard diagnostic tool for CKD, as it measures the concentration of urea, a waste product from protein metabolism, in the blood. Under normal conditions, urea is transported by the bloodstream and excreted by the kidneys, with blood levels ranging from 5 to 40 mg/dL. Levels exceeding 40 mg/dL, however, suggest impaired kidney function [11]. Regular monitoring of blood urea levels is, thus, crucial for maintaining human health. The most advanced urea sensors typically rely on colorimetric optical methods, whose benefits and drawbacks are detailed in supplemental items (SIs). While these sensors offer high sensitivity and selectivity, they require chemical reagents and enzyme immobilization, which may limit their practicality. These processes are sensitive to deposition concentrations [12] and temperature fluctuations [13], which affect enzymatic activity and hinder standardization. Additionally, the short lifespan of enzymatic reactions [14] necessitates frequent reapplication by skilled personnel, further increasing time and cost. In contrast, microwave (MW) sensors offer a promising alternative. They enable label-free detection, eliminating the need for reagents and enzymes while reducing dependency on specialized labor, lowering costs, extending sensor lifespan, and improving overall accessibility for point-of-care applications. In order to fully grasp these advantages, it is essential to understand how a material's properties vary with frequency.

Material properties such as permittivity and loss vary with frequency, directly influencing sensor resonances. Subtle changes in these properties can, however, be masked by external factors, highlighting the need for more sensitive MW sensors. Several approaches have been proposed to detect changes in dielectric properties. Antennas, for example, provide good sensitivity [15], [16], [17], but are susceptible to frequency interference [18] and environmental factors [19], reducing measurement accuracy. Waveguide sensors, in contrast, feature simple geometries with high sensitivity and strong immunity to electromagnetic interference [20]. They have been successfully employed in applications such as honey adulteration detection [21], [22] and soil classification [23]. But at low frequencies, they tend to become bulky and less portable, and their fabrication can be complex and expensive.

Microstrip sensors offer low cost, ease of fabrication, and compact size. They operate by exciting resonators whose resonances interact with the surrounding medium. Among these, the split-ring resonator (SRR) stands out for enabling materials with negative permittivity and permeability [24]. Since then, numerous resonator designs have been proposed, including ring resonators (RRs) [25], dual SRRs (DSRRs) [26], modified SRRs [27], and coplanar waveguide-based variants [28], and many others reported in the literature [29], [30], and [31].

Active SRRs (ASRRs) provide benefits such as higher sensitivity, improved resolution, and enhanced frequency stability by compensating for intrinsic losses [32], [33], [34]. These benefits, however, often come at the cost of increased complexity, size, and cost. As a result, there is growing interest in passive resonators enhanced by complementary techniques that improve sensitivity and resolution without sacrificing simplicity or cost-effectiveness. For example, [35] used a coiled capillary and recirculating signal to boost sensitivity, while [36] introduced bent grooves to enhance electric field confinement in complementary SRRs (CSRRs). In [37], an interdigital capacitor was added near the ground plane for similar effect. A CSRR-based interferometric system showed a 48-fold improvement over conventional designs [38], and [39] used a colony optimization algorithm to refine microfluidic channel routing, achieving up to 80% sensitivity gain.

In spite of these improvements, MW sensors for CKD diagnosis remain underexplored, particularly for monitoring urea in blood plasma. For example, a transmission line with a defective ground plane showed potential at 1.8 GHz in saline [40] but lacked the sensitivity required for clinically relevant urea levels. Similarly, a CSRR-based sensor was tested in simulated dialysis fluid [41] but also failed to cover the needed range. Other studies targeting urea in agricultural water [42] or protein denaturation [43] address much higher concentrations than those associated with CKD.

In view of these challenges, we propose the use of the double concentric circular SRR (DCCSRR), a design we recently developed [44]. The DCCSRR surpasses the sensitivity of current MW sensors, matching colorimetric optical sensors for low urea detection in blood plasma. It retains MW advantages by eliminating reagents and enzymes, reducing costs, simplifying fabrication, and enabling large-scale production, which is ideal for point-of-care use, especially in remote hospitals. In order to achieve these goals, we first characterized a artificial blood plasma solution (ABPS) mimicking real plasma, then enriched it with urea (ABPSU). By comparing their dielectric properties, we defined the sensor's operational frequency below 1 GHz. The DCCSRR was optimized for resonance peak and quality factor (Q) around 1 GHz. Finally, measurements with ABPSU at urea concentrations of 10–320 mg/dL showed resonance shifts around 575 MHz, exhibiting a linear response to urea levels. These findings support the development of cost-effective, high-sensitivity CKD diagnostic sensors that outperform colorimetric optical and conventional MW sensors.

The remainder of this article is organized as follows. Section II details the dielectric characterization of ABPS and ABPSU to define the operational frequency range. Section III describes the optimization of the DCCSRR response, focusing on the resonance amplitude and quality factor at low frequencies. Section IV presents the fabrication process and performance assessment of the DCCSRR under various urea concentrations. Finally, Section V concludes this article and offers final remarks. The SI provides additional details, including the experimental setup for ABPS and ABPSU characterization, a comprehensive description of the DCCSRR

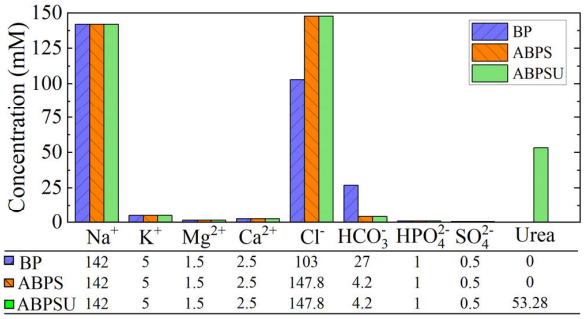

Fig. 1. Comparison between the ion concentrations found in the BP, ABPS, and ABPSU samples.

optimization process, and further information regarding DCC-SRR fabrication and performance evaluation.

II. Dielectric Characterization of ABPS and ABPSU

It is well known that every material exhibits a unique electromagnetic response characterized by its complex relative permittivity

$$\varepsilon_r(f) = \varepsilon'(f) - j\varepsilon''(f) \tag{1}$$

where $\varepsilon'(f)$ is the real part of the dielectric constant, while $\varepsilon''(f)$ is the imaginary part, representing energy losses. Dielectric characterization methods span all three states of matter, namely vapor [45], solid [46], and liquid [47]. In our study, we focus on liquids as our reference media. ABPS and ABPSU are designed to mimic the dielectric properties of blood plasma. Metallic waveguides [48] can be used for liquid characterization, but they operate within a narrow, single-mode frequency range. Another option is the substrate-integrated waveguide (SIW) based on microstrip technology [49], but its usable bandwidth is limited to the modal region. In contrast, the conventional open-ended coaxial probe method is more advantageous due to its lower cost, broader bandwidth, and high precision. Here, we use a simple open-ended coaxial cable connected to a calibrated vector network analyzer (VNA, Rohde & Schwartz ZVA-40), as described in [47]. The calibration procedure consists of measuring the reflection coefficient under three conditions: open circuit, short circuit, and with the probe immersed in a reference sample. After these calibration steps, the probe is submerged in the target fluid, and the reflection coefficient is measured again. Using these data along with the known permittivity of the reference sample, the complex permittivity of the fluid can be readily determined.

We selected ABPS as the reference medium because its electromagnetic response more closely approximates that of real blood plasma compared to deionized water (DI water), which is commonly used in the literature. ABPS was synthesized following the procedure described in [50], and its chemical composition, including ion concentrations, is compared with that of real blood plasma in Fig. 1. Note that the ion concentrations closely match those found in blood plasma, with only minor differences for Cl^- and HCO_3^-. In spite of these small deviations, ABPS reliably represents blood plasma.

The ABPSU was prepared by adding urea to the ABPS to achieve a concentration of 320 mg/dL, expressed in milimol (mM) in Table I. Although there is no universal agreement on the upper limit for urea sensing, we established three detection zones. Zone A: healthy condition (10–40 mg/dL); Zone B: unhealthy condition (40–180 mg/dL); and Zone C: Critical condition (above 180 mg/dL), indicating a high likelihood of CKD.

TABLE I
Obtained Parameters From Cole–Cole Model for ABPS and ABPSU, From 500 MHz to 10 GHz

Sample	C (mg/dL)	ε_∞	ε_s	τ (ps)	α	σ_i (S/m)	R^2
ABPS	000	76.15	3.59	9.37	0.026	1.78	0.99
APBSU	320	76.24	3.88	9.25	0.028	1.83	0.99

For the dielectric characterization of ABPS and ABPSU, we employed the experimental setup shown in Fig. S1 of the SI section, where a detailed description of the characterization procedure is also provided. In order to model the obtained complex permittivity data, we employed the Cole–Cole model, which is widely used for representing the dielectric properties of biological media. The model is mathematically expressed as follows:

$$\varepsilon^*(f) = \varepsilon_\infty + \sum_n \frac{\Delta\varepsilon_n}{1 + (j2\pi f\tau_n)^{1-\alpha_n}} + \frac{\sigma_i}{j2\pi f\varepsilon_0} \tag{2}$$

where, ε_∞ is the permittivity at high frequencies, $\Delta\varepsilon_n$ is the magnitude of dispersion, τ_n is the relaxation time constant, α_n is the dispersion-broadening parameter, and σ_i represents the static ionic conductivity. The Cole–Cole model yields an R-Squared coefficient of 0.99 for both ABPS and ABPSU, demonstrating excellent fidelity to the experimental data (see Table I for the Cole–Cole parameters). Fig. 2(a) shows the fitting results for the real part of the dielectric constant for ABPS ($\varepsilon'_{\text{fit},000}$, blue solid line) and ABPSU ($\varepsilon'_{\text{fit},320}$, red dashed line). The difference between the two ($\Delta\varepsilon' = \varepsilon'_{\text{fit},320} - \varepsilon'_{\text{fit},000}$) is minimal, particularly at low frequencies, with a slight increase observed as the frequency increases (indicated by the dotted black line). Similarly, Fig. 2(b) presents the imaginary part for ABPS ($\varepsilon''_{\text{fit},000}$, blue solid line) and ABPSU ($\varepsilon''_{\text{fit},320}$, red dashed line). As expected, the higher urea concentration in ABPSU results in increased losses up to 4 GHz (see the inset), after which the trend reverses; the dotted black line represents the difference $\Delta\varepsilon'' = \varepsilon''_{\text{fit},320} - \varepsilon''_{\text{fit},000}$. The addition of 320 mg/dL of urea to ABPS, thus, produces only modest changes in the real part of the permittivity, with a maximum variation of 0.4 at 10 GHz [Fig. 2(a)], but has a more pronounced effect on the losses, peaking at 500 MHz [Fig. 2(b)]. These results suggest that the MW sensor exhibits greater sensitivity to changes in the dielectric constant from ABPS to ABPSU at low frequencies. Furthermore, MW devices operating at lower frequencies are generally more cost effective. Consequently, to achieve high sensitivity and low cost, the DCCSRR sensor will be optimized for the low-frequency region, specifically around 1 GHz.

III. Sensor Design

We aim to detect slight urea variations in ABPSU using a DCCSRR, a modified SRR with gap extensions for improved sensitivity [51], excited by adjacent transmission lines

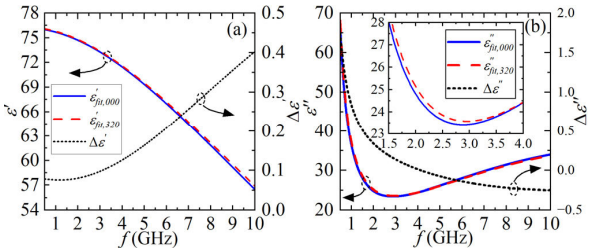

Fig. 2. Fit Relative complex permittivity for ABPS and ABPSU obtained from the Cole–Cole model after using the probe method, where (a) real dielectric constant and (b) imaginary part. In both cases, the difference between these two mediums is plotted.

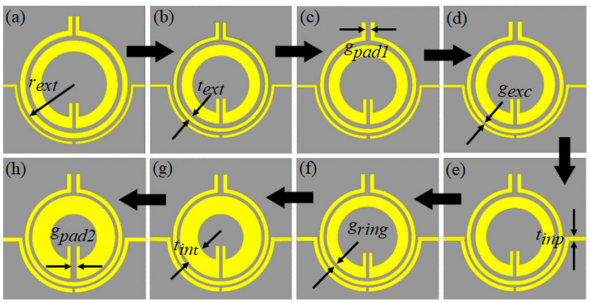

Fig. 3. Optimization of the DCCSRR, in which the resonance peak and quality factor are analyzed according to the variation of each dimension in the following order. (a) r_{ext}, (b) t_{ext}, (c) g_{pad1}, (d) g_{exc}, (e) t_{inp}, (f) g_{ring}, (g) t_{int}, and (h) g_{pad2}.

[Fig. 3(a)]. Initially set with arbitrary dimensions, the DCCSRR was optimized in Ansys HFSS [52]; details are in the SI.

Two key performance metrics guided the optimization process: the resonance peak amplitude and its quality factor (Q). The resonance amplitude is directly related to the strength of the electromagnetic fields within the sensor; higher amplitudes result in increased sensitivity. The quality factor defines the sharpness of the resonance; higher Q values enable the sensor to detect minute changes in permittivity with greater accuracy. Since the resonant behavior is strongly influenced by the sensor's dimensions, which effectively form an LC circuit, exploring a range of values for each parameter was essential for managing amplitude, frequency, and quality factors.

For optimization, each dimension shown in Fig. 3(e) was varied individually to observe its impact on the sensor's response. We adopted an optimization factor (F_{opt}) defined as the product of the resonance peak amplitude (R_p) and the quality factor (Q)

$$R_p = 10^{\max[S_{21}(\mathrm{dB})]/20} \tag{3}$$

$$F_{opt} = R_p Q. \tag{4}$$

Fig. 4 compares the sensor response before (solid black line) and after (red dashed line) the optimization process. The inset figures, labeled S_{init} and S_{opt}, display the initial and optimized geometries, respectively. Both designs were simulated on a 0.787-mm thick Rogers 5880[1] substrate ($\varepsilon_r = 2.2 - j0.002$), and the initial and final dimensions are detailed in Table II (a full description of all sensor dimensions is found in Fig. S4 and Table S1 of the SI).

The initial design was set to produce a fundamental mode in the low-frequency region, which is favorable for urea sensing. In the nonoptimized case, the sensor exhibited a resonance

[1]Trademarked.

TABLE II
INITIAL SENSOR DIMENSIONS AND THEIR FINAL VALUES AFTER OPTIMIZATION PROCESS (IN mm)

Variable	r_{ext}	t_{ext}	g_{pad1}	g_{exc}	t_{inp}	g_{ring}	t_{int}	g_{pad2}
Initial value	19	2	1	1	1	1.5	4	1
Final value	17	1.5	1.7	0.7	1.5	1	6.5	1.7

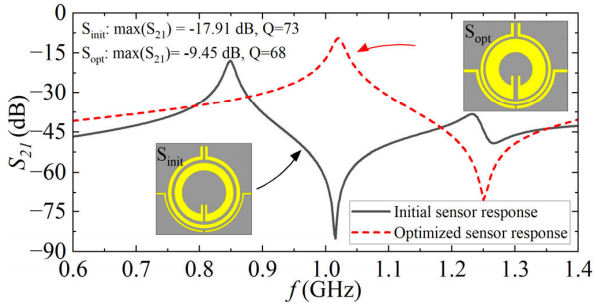

Fig. 4. Comparison between the simulated S_{21} frequency response (in magnitude) between the initial and final geometry of DCCSRR after optimizing the product of R_p and Q, in HFSS. S_{init} and S_{opt} refer to the non-optimized and optimized structures, respectively.

amplitude of −17.91 dB and a quality factor of 73, yielding $F_{opt} = 9.3$. After optimization, these parameters improved to −9.45 dB and 68, respectively, resulting in $F_{opt} = 22.9$. Although the quality factor decreased slightly, the more than doubled resonance amplitude significantly enhanced F_{opt}.

In order to detail the optimization process, Fig. 5 illustrates the sequential adjustment of each parameterized dimension of the DCCSRR, where the order of variables reflects the optimization sequence along with their respective ranges. In essence, the optimization maximizes F_{opt} by selecting the optimal combination $\max[S_{21}(\mathrm{dB})]$ and Q for each sensor dimension. Two exceptions to this protocol were made. As shown in Fig. 5(d), g_{exc} significantly influences both $\max[S_{21}(\mathrm{dB})]$ and Q. Although the maximum F_{opt} occurred at $g_{exc} = 0.5$mm, this setting drastically reduced Q; thus, to preserve the quality factor, g_{exc} was set to 0.7 mm, which, while not fully optimizing F_{opt}, maintained an acceptable Q. The highest F_{opt} for t_{inp} was achieved at 1 mm; however, this dimension is critical for impedance matching. At 1 mm, the input impedance deviates significantly from 50 Ω. By increasing t_{inp} to 1.5 mm, the impedance mismatch is minimized, although F_{opt} is not maximized. For all other parameters, the values that maximized F_{opt} were selected and are presented in Table II. Detailed F_{opt} values for each test case are provided in Fig. S3 of the SI.

With all dimensions set, the DCCSRR response was simulated from 0.5 to 3.5 GHz (Fig. 6), revealing two resonances: R_1 (optimized) and R_2. Both show field and current concentration near the external ring, with R_1 exhibiting higher intensity. The equivalent RLC circuit is detailed in the SI. The next steps include fabrication, performance evaluation, and experimental testing.

IV. FABRICATION, PERFORMANCE EVALUATION AND TESTS

Details about DCCSRR fabrication and how it was attached to the sample container are presented in the SI. Fig. 7(a) shows the mounted setup, while Fig. 7(b) presents the frequency

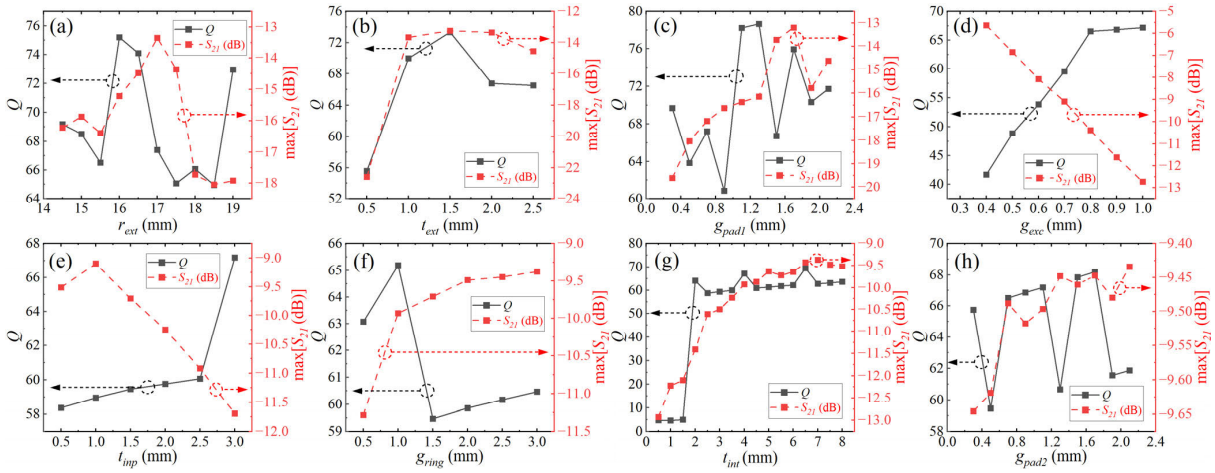

Fig. 5. Summary of the optimization process in which the product max[S_{21}(dB)] and Q of the fundamental mode resonance was maximized. The optimization order was: (a) r_{ext}, (b) t_{ext}, (c) g_{pad1}, (d) g_{exc}, (e) t_{inp}, (f) g_{ring}, (g) t_{int}, and (h) g_{pad2}.

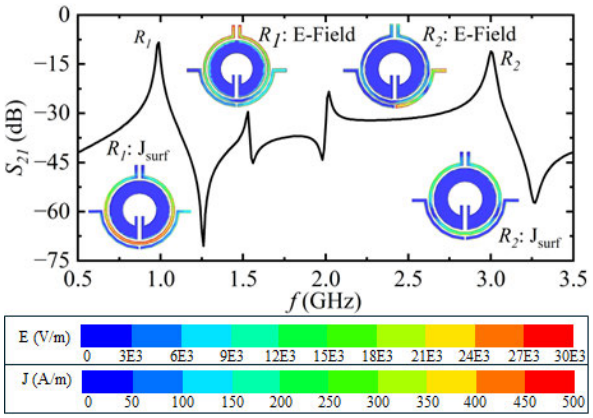

Fig. 6. HFSS simulation of the DCCSRR from 0.5 to 3.5 GHz showing the magnitude response after the optimization process. The inset figures show the electric field and surface current distributions corresponding to the resonances labeled R_1 and R_2.

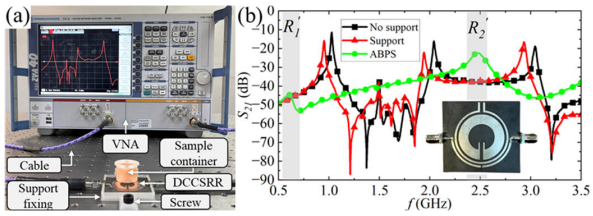

Fig. 7. Experimental setup and its corresponding responses. (a) DCCSRR connected to a VNA and fixed on the optical table through a support fixture. In (b), setup was assessed under the following situations: 1) with no support; 2) with the DCCSRR fixed between a support fixture and a sample container; and 3) with the sample container filled with ABPS, where the shaded areas highlight R_1' and R_2' (adapted from [44] under CC BY 4.0 license).

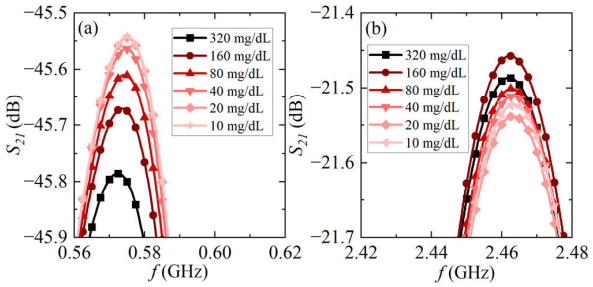

Fig. 8. Fitting of the experimental VNA data for urea concentrations in ABPS at 10, 20, 40, 80, 160, and 320 mg/dL at resonances (a), R_1' (575 MHz), and (b), R_2' (2.46 GHz), respectively.

responses for three scenarios along with an inset image of the fabricated DCCSRR. The solid black line (square marker) corresponds to the sensor without support and closely matches the simulated response. The red triangular line illustrates the influence of adding the sample container, which causes slight attenuation and redshift relative to the unsupported case. The container was positioned at the location of the highest electric field intensity, the external ring gap, as indicated by the inset in Fig. 6. Finally, when the container was filled with ABPS (green line), the sensor response changed dramatically, exhibiting only two resonances, at $R_1' = 575$ MHz and $R_2' = 2.46$ GHz, as highlighted by the shaded areas. The first resonance experienced an attenuation of approximately 30 dB, compared to about 6 dB for the second, reflecting the higher losses of ABPS at low frequencies [Fig. 2(b)].

In order to assess the DCCSRR's response to urea, ABPS samples with urea concentrations of 10, 20, 40, 80, 160, and 320 mg/dL were prepared. A minimum volume of 2 mL was used, enough to completely cover the bottom of the sample holder. For each resonant region, the VNA was configured to acquire 401 data points with an intermediate frequency (IF) bandwidth of 100 Hz. At the first resonance (R_1'), the magnitude of the frequency response varied proportionally with urea concentration, as illustrated by the fit curves in Fig. 8(a). These trends agree with those observed in Fig. 2(a) and (b), where higher concentrations produced greater redshift and attenuation. In contrast, the second resonance (R_2'), shown in Fig. 8(b), did not exhibit a proportional response across the entire concentration range. Additional experiments, shown in Fig. S5 of the SI, confirmed that R_2' was less suitable for the intended application and concentration range, so we focused exclusively on the first resonance. The SI also discusses R_1 behavior under varying permittivities.

In order to further evaluate the DCCSRR's performance at R_1', the measurements were repeated three times. Fig. 9(a) and (b) display the fit sensor's performance in terms of the magnitude at 581 MHz and the corresponding resonance frequency shift, respectively. The point at 581 MHz was selected because it exhibited the maximum amplitude within R_1', favoring the signal-to-noise ratio (SNR) within the measured range, with clear differentiation among concentrations. Notably, the sensor is capable of detecting these levels up to 620 MHz,

TABLE III
COMPARISON OF RECENTLY PUBLISHED UREA SENSORS USING SEVERAL TECHNOLOGIES

	Ref.	Operating Point λ/f *	Urea diluted in	Detection	Measured Variable	Resolution** (mg/dL)	Measured Range (mg/dL)	Measured Variable per mg/dL	Enzyme or Reagent Usage	Year
Optical colorimetric	[5] †	500 nm	Water	Smartphone	Absorbance (a.u.)	20	10-150	0.0029	Yes	2021
	[6] †	NA	Saliva	Smartphone	Green pixel intensity	~5	10-260	0.0048	Yes	2018
	[7] †	700 nm	Blood	Smartphone	RGB value	~1	0.1-150	0.0184	Yes	2025
	[10] †	585 nm	Saliva	Photodetector	Current	18	24-300	0.0019	Yes	2019
	[11] †	630 nm	Blood	Photodetector	Reflection	21	14.8-229	0.0794	Yes	2023
	[12] †	663 nm	Blood	Photodetector	Voltage (V)	10	10-50	0.00075	Yes	2024
	[11]	720 nm	Blood	Spectrometer	Wavelength (nm)	6	6-42	2.38	Yes	2023
	[15] †	766 nm	Blood	Spectrometer	Wavelength (nm)	6	6-54	0.054	Yes	2024
Microwave	[40]	1780 MHz	Saline	VNA	Frequency (MHz)	167	0-700	0.00026	No	2024
	[41]	7400 MHz	Dialysis fluid	VNA	Frequency (MHz)	40	20-100	1.875	No	2025
	[42]	2370 MHz	Water	Power detector	Amplitude (dB)	8700	$(0.22\text{-}4.35)\times10^4$	0.000032	No	2024
	[43]	1000 MHz	BSA	VNA	Amplitude (dB)	9009	0-36036	0.0000002	No	2022
	This work	**581 MHz**	**ABPS**	**VNA**	**Amplitude (dB) and frequency (MHz)**	**20**	**10-320**	**0.0092**	**No**	**2025**

* λ refers to the wavelength, while f the operation frequency; ** Minimum detectable concentration step; † Reference from SI. NA: Not Applicable.

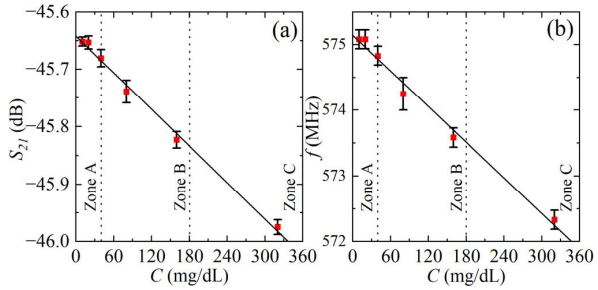

Fig. 9. Experimental data and their respective fit curves considering three measurements for the following urea concentrations in ABPSU. 10, 20, 40, 80, 160, and 320 mg/dL. In (a), amplitude values from R_1, at 581 MHz were analyzed, while in (b), its resonant frequency shift.

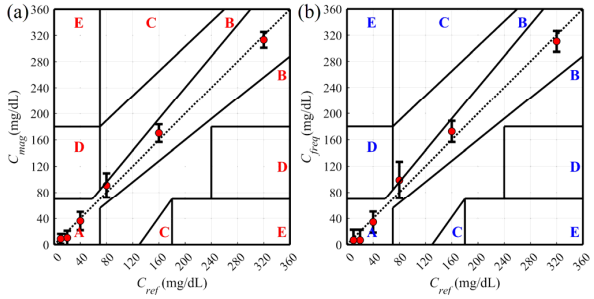

Fig. 10. CEG was used to assess the DCCSRR performance for different urea concentrations, where, in (a) amplitude of resonance at 581 MHz is evaluated, and in (b) frequency shift was considered.

demonstrating excellent performance. Overall, the DCCSRR successfully distinguishes among the three urea concentration zones, thereby supporting CKD diagnosis, and represents the first MW sensor to achieve this milestone.

For the magnitude response at 581 MHz, the fit curve exhibited linear behavior over an excursion range of approximately −0.36 dB, described by

$$\hat{y}_{\text{fit}}^{581\ \text{MHz}} = -0.001C - 46.642 \tag{5}$$

where C is the urea concentration in mg/dL. Its R-squared value is 0.995, while the mean standard deviation is $\bar{\sigma}_m = 0.0135$, indicating excellent agreement with the experimental data and low error dispersion. Similarly, the resonance frequency shift showed a linear response, given by

$$\hat{y}_{\text{fit}}^{fr} = -0.009C + 575.145. \tag{6}$$

The $R^2 = 0.989$ and $\bar{\sigma_f} = 0.162$ indicate good linearity with moderate error. A 2.75 MHz maximum shift was observed, and a Lichtenecker model (see SI) explains the R_1 shift with ABPSU concentration.

The Clarke error grid (CEG) is primarily used to assess the clinical accuracy and relevance of sensor measurements, and we have adapted it here for urea sensing. In the CEG, the x-axis represents reference values, while the y-axis represents the sensor's predictions. The grid is divided into five regions (A through E), with Region A corresponding to measurements within a ±20% deviation from the reference (the most desirable outcome). Regions B through E represent progressively larger errors that could lead to incorrect or harmful treatment. Fig. 10(a) shows that when using amplitude variation for urea prediction, 94.4% of the data fell within Region A and 5.6% in Region B. In contrast, Fig. 10(b), which considers frequency shift, shows that 77.8% of the data lies within Region A. Overall, the DCCSRR showed good performance, with amplitude variation yielding superior accuracy. The main drawback of the DCCSRR is the sample container, which needs thorough cleaning to avoid cross-contamination.

Table III compares state-of-the-art sensors based on different operating principles, dividing them into optical colorimetric sensors and MW sensors. Optical colorimetric sensors offer high resolution due to their use of enzymes and chemical reagents. In contrast, while MW sensors have not yet been applied to urea detection in blood sensors, they offer significant advantages, including low cost, long lifespan (owing to their independence from enzymes and reagents), and ease of fabrication for large-scale production. The DCCSRR leverages these benefits while maintaining sufficient sensitivity to detect subtle urea variations in ABPS. The DCCSRR was, moreover, able to detect urea concentrations in spite of interference

from varying glucose levels, as detailed in the SI. These achievements position the DCCSRR as the first MW sensor capable of diagnosing CKD with a resolution comparable to that of optical colorimetric sensors.

V. Conclusion

In this article, we presented the first MW device capable of detecting urea concentrations in ABPSU at levels relevant for CKD diagnosis. We began by employing the conventional open-ended probe method to extract the complex relative permittivity of ABPS and ABPSU, characterizing their electromagnetic properties over a frequency range of 500 MHz to 10 GHz. Our findings indicated that the difference in ε' between the two samples is more pronounced at high frequencies, whereas the difference in ε'' is more significant at low frequencies. This observation guided us in designing the sensor for low-frequency operation, prioritizing the loss effects over the dielectric constant, while also benefiting from the lower cost of MW components at these frequencies.

Then, we optimized the DCCSRR for urea determination in ABPS aimed at CKD diagnosis. We detailed the optimization process, focusing on simultaneously improving Q and the resonance magnitude at low frequencies (specifically around 1 GHz), which had not been previously explored. When exposed to ABPSU, the optimized resonance redshifts to 575 MHz, enabling the detection of urea concentrations ranging from 10 to 320 mg/dL. The sensor's response is linear for both amplitude and frequency shifts, with a resolution of 20 mg/dL and no overlapping errors. In contrast to optical sensors, which rely on enzymes and reagents and suffer from limited lifespan, the proposed MW sensor offers several advantages, including extended operational life, ease of use, and low cost, while maintaining sensitivity comparable to that of optical systems. These results highlight the potential of MW sensor technology for precise urea measurement in clinical settings, indicating a promising avenue for its integration into routine diagnostic applications.

References

[1] P. Rossing, T. W. Hansen, and T. Kümler, "Cardiovascular and non-renal complications of chronic kidney disease: Managing risk," *Diabetes Obes Metab*, vol. 26, no. S6, pp. 13–21, Jul. 2024.

[2] K. J. Jager, C. Kovesdy, R. Langham, M. Rosenberg, V. Jha, and C. Zoccali, *A Single Number for Advocacy and Communication-Worldwide More Than 850 Million Individuals Have Kidney Diseases*. London, U.K.: Oxford Univ. Press, 2019.

[3] K. J. Foreman et al., "Forecasting life expectancy, years of life lost, and all-cause and cause-specific mortality for 250 causes of death: Reference and alternative scenarios for 2016–40 for 195 countries and territories," *Lancet*, vol. 392, no. 10159, pp. 2052–2090, Oct. 2018.

[4] P. K.-T. Li et al., "Tackling dialysis burden around the world: A global challenge," *Kidney Diseases*, vol. 7, no. 3, pp. 167–175, 2021.

[5] E. D. Poggio, J. J. Augustine, S. Arrigain, D. C. Brennan, and J. D. Schold, "Long-term kidney transplant graft survival—Making progress when most needed," *Amer. J. Transplantation*, vol. 21, no. 8, pp. 2824–2832, Aug. 2021.

[6] S. Gooran, A. Javid, and G. Pourmand, "Delayed hemorrhage in kidney transplantation: A life-threatening condition," *Int. J. Organ. Transplant. Med.*, vol. 9, no. 1, pp. 46–49, Jan. 2018.

[7] A. Agrawal, M. G. Ison, and L. Danziger-Isakov, "Long-term infectious complications of kidney transplantation," *Clin. J. Amer. Soc. Nephrol.*, vol. 17, no. 2, pp. 286–295, 2022.

[8] H. Oweira et al., "Risk factors of rejection in renal transplant recipients: A narrative review," *J. Clin. Med.*, vol. 11, no. 5, p. 1392, Mar. 2022.

[9] M. Hueso, E. Navarro, D. Sandoval, and J. M. Cruzado, "Progress in the development and challenges for the use of artificial kidneys and wearable dialysis devices," *Kidney Diseases*, vol. 5, no. 1, pp. 3–10, 2019.

[10] B. Caplin, S. Kumar, and A. Davenport, "Patients' perspective of haemodialysis-associated symptoms," *Nephrology Dialysis Transplantation*, vol. 26, no. 8, pp. 2656–2663, Aug. 2011.

[11] L. Cheng, W. Zheng, Y.-N. Zhang, X. Li, and Y. Zhao, "Highly sensitive fiber-optic SPR urea sensor based on ZIF-8/urease," *IEEE Trans. Instrum. Meas.*, vol. 72, pp. 1–7, 2023.

[12] A. Sassolas, L. J. Blum, and B. D. Leca-Bouvier, "Immobilization strategies to develop enzymatic biosensors," *Biotechnol. Adv.*, vol. 30, no. 3, pp. 489–511, May 2012.

[13] U. B. Trivedi et al., "Potentiometric biosensor for urea determination in milk," *Sens. Actuators B, Chem.*, vol. 140, no. 1, pp. 260–266, Jun. 2009.

[14] T. Q. N. Tran, G. Das, and H. H. Yoon, "Nickel-metal organic framework/MWCNT composite electrode for non-enzymatic urea detection," *Sens. Actuators B, Chem.*, vol. 243, pp. 78–83, May 2017.

[15] C. Zhang et al., "A compact high sensitivity antenna sensor based on spoof LSPs for ethanol sensing," *IEEE Sensors J.*, vol. 24, no. 24, pp. 40791–40800, Oct. 2024.

[16] T. Alam and M. Cheffena, "Integrated microwave antenna/sensor for sensing and communication applications," *IEEE Trans. Microw. Theory Techn.*, vol. 70, no. 11, pp. 5289–5300, Nov. 2022.

[17] A. Kandwal et al., "Young's double slit method-based higher order mode surface plasmon microwave antenna sensor: Modeling, measurements, and application," *IEEE Trans. Instrum. Meas.*, vol. 71, pp. 1–11, 2022.

[18] Z. Zhou, P. Li, M. Sheng, Q. Zhou, and P. Hu, "Ambient interferences suppressing for in-situ radiated emissions measurement based on array signal processing and adaptive noise cancellation," *IEEE Trans. Electromagn. Compat.*, vol. 62, no. 4, pp. 1055–1067, Aug. 2020.

[19] Z. U. Islam, A. Bermak, and B. Wang, "A review of microstrip patch antenna-based passive sensors," *Sensors*, vol. 24, no. 19, p. 6355, Sep. 2024.

[20] C.-J. Chung et al., "Silicon-based hybrid integrated photonic chip for K_u band electromagnetic wave sensing," *J. Lightw. Technol.*, vol. 36, no. 9, pp. 1568–1575, May 15, 2018.

[21] H. Hasar et al., "Prediction of water-adulteration within honey by airline de-embedding waveguide measurements," *Measurement*, vol. 179, Jul. 2021, Art. no. 109469.

[22] H. Hasar et al., "Sensitive microwave sensor for detection and quantification of water in adulterated honey," *IEEE Trans. Instrum. Meas.*, vol. 74, pp. 1–13, 2025.

[23] P. R. Sagar and P. N. Patel, "Metamaterial integrated rectangular waveguide with EM-wave localization for dielectric & moisture estimation of soil," *IEEE Sensors J.*, vol. 21, no. 20, pp. 22661–22669, Oct. 2021.

[24] J. B. Pendry, A. J. Holden, D. J. Robbins, and W. J. Stewart, "Magnetism from conductors and enhanced nonlinear phenomena," *IEEE Trans. Microw. Theory Techn.*, vol. 47, no. 11, pp. 2075–2084, Nov. 1999.

[25] N. Hosseini, M. Baghelani, and M. Daneshmand, "Selective volume fraction sensing using resonant-based microwave sensor and its harmonics," *IEEE Trans. Microw. Theory Techn.*, vol. 68, no. 9, pp. 3958–3968, Sep. 2020.

[26] S. Kiani, P. Rezaei, and M. Navaei, "Dual-sensing and dual-frequency microwave SRR sensor for liquid samples permittivity detection," *Measurement*, vol. 160, Aug. 2020, Art. no. 107805.

[27] N. Hosseini and M. Baghelani, "Selective real-time non-contact multivariable water-alcohol-sugar concentration analysis during fermentation process using microwave split-ring resonator based sensor," *Sens. Actuators A, Phys.*, vol. 325, Jul. 2021, Art. no. 112695.

[28] N. Hosseini, S. S. Olokede, and M. Daneshmand, "A novel miniaturized asymmetric CPW split ring resonator with extended field distribution pattern for sensing applications," *Sens. Actuators A, Phys.*, vol. 304, Apr. 2020, Art. no. 111769.

[29] S. Kiani, P. Rezaei, and M. Fakhr, "Real-time measurement of liquid permittivity through label-free meandered microwave sensor," *IETE J. Res.*, vol. 70, no. 5, pp. 4606–4616, May 2024.

[30] S. Kiani, P. Rezaei, and M. Fakhr, "Dual-frequency microwave resonant sensor to detect noninvasive glucose-level changes through the fingertip," *IEEE Trans. Instrum. Meas.*, vol. 70, pp. 1–8, 2021.

[31] S. Kiani and P. Rezaei, "Microwave substrate integrated waveguide resonator sensor for non-invasive monitoring of blood glucose concentration: Low cost and painless tool for diabetics," *Measurement*, vol. 219, Sep. 2023, Art. no. 113232.

[32] M. Abdolrazzaghi, M. H. Zarifi, C. F. A. Floquet, and M. Daneshmand, "Contactless asphaltene detection using an active planar microwave resonator sensor," *Energy Fuels*, vol. 31, no. 8, pp. 8784–8791, Aug. 2017.

[33] M. Abdolrazzaghi, N. Katchinskiy, A. Y. Elezzabi, P. E. Light, and M. Daneshmand, "Noninvasive glucose sensing in aqueous solutions using an active split-ring resonator," *IEEE Sensors J.*, vol. 21, no. 17, pp. 18742–18755, Sep. 2021.

[34] M. Abdolrazzaghi and M. Daneshmand, "Dual active resonator for dispersion coefficient measurement of Asphaltene nano-particles," *IEEE Sensors J.*, vol. 17, no. 22, pp. 7248–7256, Nov. 2017.

[35] M. I. O. Souza, A. F. D. Mota, V. M. Pepino, J. P. Carmo, and B. V. Borges, "Multi-purpose microwave biosensor based on signal encoding technique and microfluidics for improved sensitivity," *IEEE Sensors J.*, vol. 21, no. 4, pp. 4571–4581, Feb. 2021.

[36] X. Han, K. Liu, and S. Zhang, "High-sensitivity dual-band microfluidic microwave sensor for liquid dielectric characterization," *IEEE Sensors J.*, vol. 24, no. 22, pp. 36689–36697, Nov. 2024.

[37] W. Ye, D.-W. Wang, J. Wang, S. Chen, G. Wang, and W.-S. Zhao, "An ultrahigh-sensitivity dual-mode microwave sensor for microfluidic applications," *IEEE Microw. Wireless Technol. Lett.*, vol. 33, no. 7, pp. 1082–1085, Jul. 2023.

[38] C. Jang, J.-K. Park, H.-J. Lee, G.-H. Yun, and J.-G. Yook, "Sensitivity-enhanced fluidic glucose sensor based on a microwave resonator coupled with an interferometric system for noninvasive and continuous detection," *IEEE Trans. Biomed. Circuits Syst.*, vol. 15, no. 5, pp. 1017–1026, Oct. 2021.

[39] W.-S. Zhao, B.-X. Wang, D.-W. Wang, B. You, Q. Liu, and G. Wang, "Swarm intelligence algorithm-based optimal design of microwave microfluidic sensors," *IEEE Trans. Ind. Electron.*, vol. 69, no. 2, pp. 2077–2087, Feb. 2022.

[40] S. Hosseinzadeh and M. Yousefi, "A permittivity and conductivity sensor based on microstrip transmission line with defective ground for detection of urea in saline," *IEEE Trans. Instrum. Meas.*, vol. 73, pp. 1–11, 2024.

[41] S. R. Charvadeh, J. Ghalibafan, A. Abbasi, A. Haidary, and E. Salimi, "Utilization of the dialysate to characterize dialysis adequacy by using microwave urea biosensor based on complementary split-ring resonator (CSRR)," *Measurement*, vol. 241, Feb. 2025, Art. no. 115703.

[42] Z.-Y. Lim, H. K. Mun, J.-H. Low, B.-H. Kwan, and C.-H. Tan, "A two-port microwave sensor for real-time liquid fertilizer concentration measurement system with Internet of Things," *Comput. Electron. Agricult.*, vol. 226, Nov. 2024, Art. no. 109460.

[43] J. Mu noz-Enano, O. Peytral-Rieu, P. Vélez, D. Dubuc, K. Grenier, and F. Martín, "Characterization of the denaturation of Bovine Serum Albumin (BSA) protein by means of a differential-mode microwave microfluidic sensor based on slot resonators," *IEEE Sensors J.*, vol. 22, no. 14, pp. 14075–14083, Jul. 2022.

[44] M. I. O. Souza, N. M. Santos, J. C. P. Alarcon, L. C. Varanda, V. M. Pepino, and B.-H.-V. Borges, "Microwave glucose sensing using double circular split ring resonators for improved sensitivity: The role of artificial blood plasma and deionized water," *IEEE Sensors J.*, vol. 25, no. 3, pp. 4529–4540, Feb. 2025.

[45] M. G. Hopkins, Y. Leusmann, M. Richter, E. F. May, and P. L. Stanwix, "Characterization of fluid-phase behavior using an advanced microwave re-entrant cavity," *J. Chem. Eng. Data*, vol. 65, no. 7, pp. 3393–3402, Jul. 2020.

[46] P. Vélez et al., "Single-frequency amplitude-modulation sensor for dielectric characterization of solids and microfluidics," *IEEE Sensors J.*, vol. 21, no. 10, pp. 12189–12201, May 2021.

[47] J. Z. Bao, C. C. Davis, and M. L. Swicord, "Microwave dielectric measurements of erythrocyte suspensions," *Biophysical J.*, vol. 66, no. 6, pp. 2173–2180, Jun. 1994.

[48] Y. Shimizu, N. Ishii, T. Nagaoka, and S. Watanabe, "Measurement method for dielectric property of lossy liquid using waveguide well for SAR probe calibration," *IEEE Trans. Instrum. Meas.*, vol. 72, pp. 1–12, 2023.

[49] A. Hamid Allah, G. A. Eyebe, and F. Domingue, "Fully 3D-printed microfluidic sensor using substrate integrated waveguide technology for liquid permittivity characterization," *IEEE Sensors J.*, vol. 22, no. 11, pp. 10541–10550, Jun. 2022.

[50] A. Oyane, H.-M. Kim, T. Furuya, T. Kokubo, T. Miyazaki, and T. Nakamura, "Preparation and assessment of revised simulated body fluids," *J. Biomed. Mater. Res. A*, vol. 65A, no. 2, pp. 188–195, May 2003.

[51] N. Sharafadinzadeh, M. Abdolrazzaghi, and M. Daneshmand, "Highly sensitive microwave split ring resonator sensor using gap extension for glucose sensing," in *IEEE MTT-S Int. Microw. Symp. Dig.*, Sep. 2017, pp. 1–3.

[52] *HFSS: High Frequency Structure Simulator*, ANSYS, Canonsburg, PA, USA, Jan. 2024. [Online]. Available: https://www.ansys.com/

Mateus I.O. Souza was born in Ribeirão Preto, Brazil, in January 1991. He received the B.Sc. degree in electrical engineering from the Universidade Federal do Triângulo Mineiro (UFTM), Uberaba, Brazil, in 2017, and the M.Sc. degree in electrical engineering from the School of Engineering, University of São Paulo (EESC/USP), São Carlos, Brazil, in 2020, where he is currently pursuing the Ph.D. degree in telecommunications.

His research interests include the design of microstrip RF structures, biosensors, signal processing, and machine learning techniques.

Natália M. Santos was born in Rancharia, Brazil, in May 1994. She received the B.Sc. degree from the Universidade Estadual Paulista (FCT/UNESP), Presidente Prudente, Brazil, in 2019, and the M.Sc. degree in physical chemistry from the Institute of Chemistry, University of São Paulo (IQSC, USP), São Carlos, Brazil, in 2021, where she is currently pursuing the Ph.D. degree in physical chemistry.

Her research interests include the synthesis of nanomaterials with magnetic and optical Properties, modification and functionalization of nanostructures for biomedical applications, and colloidal study of nanomaterials.

Laudemir C. Varanda received the B.Sc., M.Sc., and Ph.D. degrees in chemistry (physical chemistry) from the Chemistry Institute of Araraquara – UNESP, Presidente Prudente, Brazil, in 1996, 1999, and 2003, respectively.

He completed an internship at the Instituto de Ciencia de Materiales de Madrid - ICMM, Madrid, Spain from 2000 to 2001. He was a Postdoctoral Researcher in materials chemistry with UNESP from 2004 to 2006. Today, he is a Professor with the Chemistry Institute of São Carlos, University of São Paulo (USP), São Carlos, Brazil, since 2007. His current research interests include syntheses, characterization, and self-assembly of nanostructured materials with magnetic, optical, and electronic properties for biomedical, environment, catalysis, sensors, biosensors, and energy applications.

Vinicius M. Pepino received the Ph.D. degree in electrical engineering from the University of São Paulo, São Carlos, Brazil, in 2023.

He is currently a Professor with the Department of Electrical Engineering and Computing (SEL), EESC/USP. His research interests include photonics, microwaves, and metasurfaces within the metamaterials group: microwaves and optics (GMeta), with emphasis on holography, biosensors, and devices for communications.

Ben-Hur V. Borges received the Ph.D. degree in electrical engineering from Drexel University, Philadelphia, PA, USA, in 1997.

From 1997 to 1998, he was a Postdoctoral Researcher with São Carlos School of Engineering, University of São Paulo, São Carlos, Brazil. In 2005, he became an Associate Professor with the Department of Electrical and Computer Engineering, School of Engineering, University of São Paulo (SEL/EESC/USP). Since 2018, he has been a Full Professor at SEL/EESC/USP. He is the Director of the metamaterials group: microwave and optics (GMeta). His research interests include metamaterials and metasurfaces for microwave and optical applications, nanoplasmonics, the design and characterization of devices for communications and sensing applications, and the modeling of optical code multiple access networks.

Dr. Borges is an Editorial Board Member of the *Journal of Physics: Photonics*.

Coordenação de Aperfeiçoamento de Pessoal de Nível Superior (CAPES) - ROR identifier: 00x0ma614